# Implicit–Explicit Multistep Methods for Fast-Wave–Slow-Wave Problems

DALE R. DURRAN AND PETER N. BLOSSEY

*University of Washington, Seattle, Washington*

(Manuscript received 30 March 2011, in final form 22 September 2011)

ABSTRACT

Implicit–explicit (IMEX) linear multistep methods are examined with respect to their suitability for the integration of fast-wave–slow-wave problems in which the fast wave has relatively low amplitude and need not be accurately simulated. The widely used combination of trapezoidal implicit and leapfrog explicit differencing is compared to schemes based on Adams methods or on backward differencing. Two new families of methods are proposed that have good stability properties in fast-wave–slow-wave problems: one family is based on Adams methods and the other on backward schemes. Here the focus is primarily on four specific schemes drawn from these two families: a pair of Adams methods and a pair of backward methods that are either (i) optimized for third-order accuracy in the explicit component of the full IMEX scheme, or (ii) employ particularly good schemes for the implicit component. These new schemes are superior, in many respects, to the linear multistep IMEX schemes currently in use.

The behavior of these schemes is compared theoretically in the context of the simple oscillation equation and also for the linearized equations governing stratified compressible flow. Several schemes are also tested in fully nonlinear simulations of gravity waves generated by a localized source in a shear flow.

## 1. Introduction

The atmosphere and the ocean support several different types of waves that propagate at very different speeds. If time derivatives in the equations governing atmospheric flow are approximated using explicit finite-difference schemes, the maximum stable time step will be limited by the speed of the fastest-moving wave. Yet the fastest-moving atmospheric and oceanic waves are sound waves, which play no direct role in atmospheric and ocean circulations and do not need to be accurately simulated.

Atmospheric models typically avoid the severe time-step restrictions associated with sound wave propagation in one of three ways. One approach is to replace the governing equations with an approximate system, such as the anelastic (Ogura and Phillips 1962; Lipps and Hemler 1982; Bannon 1996), or pseudo-incompressible equations (Durran 1989, 2008), before constructing any numerical approximations. The other two approaches approximate the full compressible equations using numerical techniques that treat sound waves in a stable, but inaccurate manner, while faithfully approximating the behavior of the slower-moving waves. This may be accomplished either by resorting to implicit time differencing (Tapp and White 1976) or by splitting up the terms in the governing equations and integrating those responsible for sound wave propagation on a smaller time step than that used for the remaining terms (Klemp and Wilhelmson 1978; Tatsumi 1983; Wicker and Skamarock 2002).

Fully implicit time differences require the solution of a nonlinear algebraic system at each time step, and while they continue to be the subject of ongoing investigation (Evans et al. 2010), they are generally thought to be less efficient than implicit–explicit (IMEX) methods (also known as semi-implicit methods) in which only those terms responsible for linear sound wave propagation are evaluated using implicit differences and the remaining terms are integrated using explicit formulas. A large body of research exists on the construction of IMEX methods for advection-diffusion problems, in which the diffusion terms are treated implicitly and the advection terms with some type of explicit differencing (Varah 1980; Ascher et al. 1995). Less attention has been devoted to the development of IMEX methods for fast-wave–slow-wave problems, but at least in atmospheric science, a basic

*Corresponding author address:* Dale R. Durran, Dept. of Atmospheric Sciences, University of Washington, Box 351640, Seattle, WA 98195-1640.
E-mail: drdee@uw.edu

DOI: 10.1175/MWR-D-11-00088.1

TABLE 1. Coefficients of implicit–explicit multistep methods following (2). In the first column, values of $c$ are given for implicit Adams (5) and backward (6) methods. The values of $b$ are listed for explicit Adams (10) and backward (11) schemes.

| Method | | | | | | | | | | |
|---|---|---|---|---|---|---|---|---|---|---|
| Implicit | Explicit | $\alpha_1$ | $\alpha_0$ | $\alpha_{-1}$ | $\beta_0$ | $\beta_{-1}$ | $\beta_{-2}$ | $\nu_1$ | $\nu_0$ | $\nu_{-1}$ |
| T2$\theta$ | LF | 1/2 | 0 | −1/2 | 1 | 0 | 0 | $\theta$ | 0 | 1–$\theta$ |
| T1 | AB3 | 1 | −1 | 0 | 23/12 | −4/3 | 5/12 | 1/2 | 1/2 | 0 |
| MCN ($c$ = 1/8) | AX2+ ($b$ = 3/8) | 1 | −1 | 0 | 27/16 | −7/8 | 3/16 | 9/16 | 3/8 | 1/16 |
| AM2* ($c$ = 1/2) | AX2* ($b$ = 1/2) | 1 | −1 | 0 | 7/4 | −1 | 1/4 | 3/4 | 0 | 1/4 |
| AI2* ($c$ = 3/2) | AB3 ($b$ = 5/6) | 1 | −1 | 0 | 23/12 | −4/3 | 5/12 | 5/4 | −1 | 3/4 |
| BDF2 ($c$ = 0) | BX2 ($b$ = 0) | 3/2 | −2 | 1/2 | 2 | −1 | 0 | 1 | 0 | 0 |
| BDF2 ($c$ = 0) | BX2* ($b$ = 1/2) | 3/2 | −2 | 1/2 | 5/2 | −2 | 1/2 | 1 | 0 | 0 |
| BI2* ($c$ = 1/3) | BX3* ($b$ = 2/3) | 3/2 | −2 | 1/2 | 8/3 | −7/3 | 2/3 | 4/3 | −2/3 | 1/3 |

leapfrog-trapezoidal IMEX method (see first line of Table 1) is widely used (Kwizak and Robert 1971).

Consistent with the true solution, pure IMEX leapfrog-trapezoidal approximations to inviscid linear wave-propagation problems neither damp nor amplify the numerical solution. In practical applications, however, the leapfrog-trapezoidal method requires some modifications. The computational mode of the explicit leapfrog scheme is undamped and may interact with the physical mode in nonlinear problems to produce spurious $2\Delta t$ oscillations (time splitting); Robert–Asselin (RA) filtering (Robert 1966; Asselin 1972) or Robert–Asselin–Williams (RAW) filtering (Williams 2009) is often applied to avoid this problem. In addition, the weights in the trapezoidal integration formula are sometimes backward biased in an effort to enhance the stability of the implicit part (Benoit et al. 1997), by choosing $\frac{1}{2} < \theta \leq 1$ in the formula given on the first line of Table 1. Either filtering or off-centering the integration weights render these methods first-order accurate. In addition the off-centering damps a rather wide range of frequencies, including those that are rather well resolved. Can we do better?

The leapfrog-trapezoidal method is a linear multistep IMEX method. In the following we explore several other linear multistep methods that lend themselves to IMEX differencing in fast-wave–slow-wave problems while producing more scale-selective damping at the highest frequencies. These methods permit almost the same maximum stable time step allowed by the filtered IMEX leapfrog-trapezoidal methods while achieving higher accuracy.

## 2. Formulation of IMEX multistep methods

The equations governing atmospheric or ocean dynamics (and many other processes) can be expressed in the following form:

$$\frac{\partial \mathbf{u}}{\partial t} = \mathbf{f}(\mathbf{u}) + \mathbf{L}\mathbf{u}, \tag{1}$$

where $\mathbf{u}$ is the state variable, $\mathbf{L}$ is the matrix associated with a linear operator that includes processes with short time scales (such as sound and/or gravity wave propagation), and all remaining terms are collected in $\mathbf{f}(\mathbf{u})$, including those responsible for advection. If the terms supporting the fast processes are not linear, they may be linearized to form $\mathbf{L}$, and the remaining nonlinear contributions may be incorporated in $\mathbf{f}$.

Letting $\mathbf{q}^n$ be the numerical approximation to $\mathbf{u}$ at time $n\Delta t$, a linear IMEX $M + 1$ step approximation to (1) may be expressed in the following form:

$$\sum_{k=-M}^{1} \alpha_k \mathbf{q}^{n+k} = \Delta t \left[ \sum_{k=-M}^{0} \beta_k \mathbf{f}(\mathbf{q}^{n+k}) + \sum_{k=-M}^{1} \nu_k \mathbf{L}\mathbf{q}^{n+k} \right]. \tag{2}$$

The set of coefficients $(\alpha_k, \beta_k)$ define the explicit method, whereas the implicit portion is defined by the set $(\alpha_k, \nu_k)$. The use of a single set of $\alpha_k$ restricts the choice of explicit and implicit multistep methods that can be combined in the IMEX scheme to those with identical $\alpha_k$.

### a. The implicit component

To ensure that the time step is not restricted by the fast processes, the implicit method should be $A$ stable, although as shown by Dahlquist (1963) no $A$-stable linear multistep method can be higher than second-order accurate. A method is $A$ stable if when applied to the scalar problem

$$\frac{du}{dt} = \eta u, \tag{3}$$

with $u$ and $\eta$ complex, and $\Re(\eta) \leq 0$, the magnitude of the factor by which the numerical solution amplifies

each time step, $|A| \equiv |q^{n+1}/q^n|$, is bounded by unity regardless of the size of the time step (Durran 2010, p. 41).[1] When IMEX methods are used in advection-diffusion problems, the implicit method typically has the additional property that it is $L$ stable. An $L$-stable method is an $A$-stable method satisfying the additional condition that $|A| \to 0$ as $\Re(\eta)\Delta t \to -\infty$ (Durran 2010, p. 48). Integrating the diffusion terms with an $L$-stable method ensures that very short wavelength features decay properly when the time step and the diffusivities are large. Some damping of the highest frequencies has also proved helpful in many fast-wave–slow-wave problems, so here our primary focus will be on implicit methods that provide such damping, although we will not necessarily require $|A| \to 0$ as $\Im(\eta)\Delta t \to \pm\infty$.

One set of potentially attractive candidates for use in linear IMEX multistep methods are the Adams schemes for which $\alpha_1 = 1$, $\alpha_0 = -1$ and $\alpha_k = 0$ for $-M \le k < 0$. The highest-order explicit Adams scheme that can be obtained using $s$ steps is the $s$-step Adams–Bashforth method; the highest-order implicit scheme is the $s$-step Adams–Moulton method. Adams–Moulton implicit schemes are, however, of limited use in IMEX formulations because the only $A$-stable Adams–Moulton method is the classic one-step trapezoidal scheme (denoted here as T1), which does not damp high-frequency oscillations. We will therefore consider Adam's methods whose order of accuracy is lower than the best that can be achieved using a given number of time steps, but whose stability properties nevertheless make them potentially attractive choices for IMEX approximations to fast-wave–slow-wave problems.

The simplest example of such a method may be obtained from the trapezoidal scheme, which may be modified to produce frequency-dependent damping by off-centering it in time; the result is a first-order one-step scheme. When used in conjunction with an explicit leapfrog scheme, the time differencing in the two schemes is made compatible by approximating the trapezoidal difference over $2\Delta t$ (in which case it is not formally an Adams scheme). The result is

$$\frac{\mathbf{q}^{n+1} - \mathbf{q}^{n-1}}{2\Delta t} = \theta \mathbf{L}\mathbf{q}^{n+1} + (1 - \theta)\mathbf{L}\mathbf{q}^{n-1}, \qquad (4)$$

with $1/2 < \theta \le 1$. Choosing $\theta$ near ½ gives the best accuracy, but only weak damping. We will refer to this scheme as T2$\theta$.

Second-order accuracy can be achieved using a member of the following one-parameter family of implicit Adams methods, which are $A$ stable for any nonnegative $c$ (Frank et al. 1997):

$$\frac{\mathbf{q}^{n+1} - \mathbf{q}^{n}}{\Delta t} = \frac{1}{2}(1 + c)\mathbf{L}\mathbf{q}^{n+1} + \frac{1}{2}(1 - 2c)\mathbf{L}\mathbf{q}^{n} + \frac{c}{2}\mathbf{L}\mathbf{q}^{n-1}. \qquad (5)$$

Choosing $c = 0$ reduces this to a two-step method and gives the familiar trapezoidal scheme. The case $c = ½$ yields the method denoted AM2* by Fornberg and Driscoll (1999), who used it in conjunction with a fourth-order Adams-Bashforth method for IMEX simulations of dispersive waves. Nevanlinna and Liniger (1978) found AM2* to be the two-step second-order method that gave the smallest error bounds among all methods that yield nongrowing solutions to a test problem similar to (3) with $\eta(t) \le \eta_0 < 0$ for $t \ge 0$.

Instead of Adams methods, one could alternatively consider the one-parameter family of backward methods:

$$\frac{\frac{3}{2}\mathbf{q}^{n+1} - 2\mathbf{q}^{n} + \frac{1}{2}\mathbf{q}^{n-1}}{\Delta t} = (1 + c)\mathbf{L}\mathbf{q}^{n+1} - 2c\mathbf{L}\mathbf{q}^{n} + c\mathbf{L}\mathbf{q}^{n-1}. \qquad (6)$$

The left-hand side is the standard second-order backward-difference approximation to the derivative at time level $n + 1$ and the right-hand side is a second-order approximation to $\mathbf{Lq}$ at time $n + 1$. The familiar $L$-stable second-order backward difference formula (BDF2) is obtained by choosing $c = 0$. Numerical evaluations of the amplification factor $A$ show the family schemes (6) to be $A$ stable for $c \ge -¼$.

The amplification factors $A$ generated by several of the preceding implicit methods are compared with that for the exact solution to (3) in Fig. 1. Each panel shows contours of $|A|$ plotted as a function of $\Re(\eta)\Delta t$ and $\Im(\eta)\Delta t$. Method AI2* is (5) with $c = 3/2$, method BI2* is (6) with $c = 1/3$; the significance of these methods will be discussed in section 3.

As expected for $A$-stable methods, $|A| \le 1$ throughout the half-plane $\Re(\eta)\Delta t \le 0$. One limiting behavior is exhibited by the T2$\theta$ method with $\theta = 0.5$, which correctly preserves the amplitude of purely oscillatory solutions, but fails to correctly damp the solution if $\Re(\eta)\Delta t \ll -1$. The other limit is attained by the BDF2 method, which consistent with its $L$ stability, provides the best treatment of the strongly damped case [$\Re(\eta)\Delta t \ll -1$]. Most of the other methods produce significant damping as $\Re(\eta)\Delta t \to -\infty$ (the values of $|A|$ in this limit appear in the bottom-left corner of each panel of Fig. 1), and like

[1] An $N$-step linear multistep method has $N$ amplification factors, one of which corresponds to the physical mode. The others are associated with computational modes. Unless otherwise specified, $|A|$ will refer to the maximum of the magnitude of the amplification factor over all physical and computational modes.

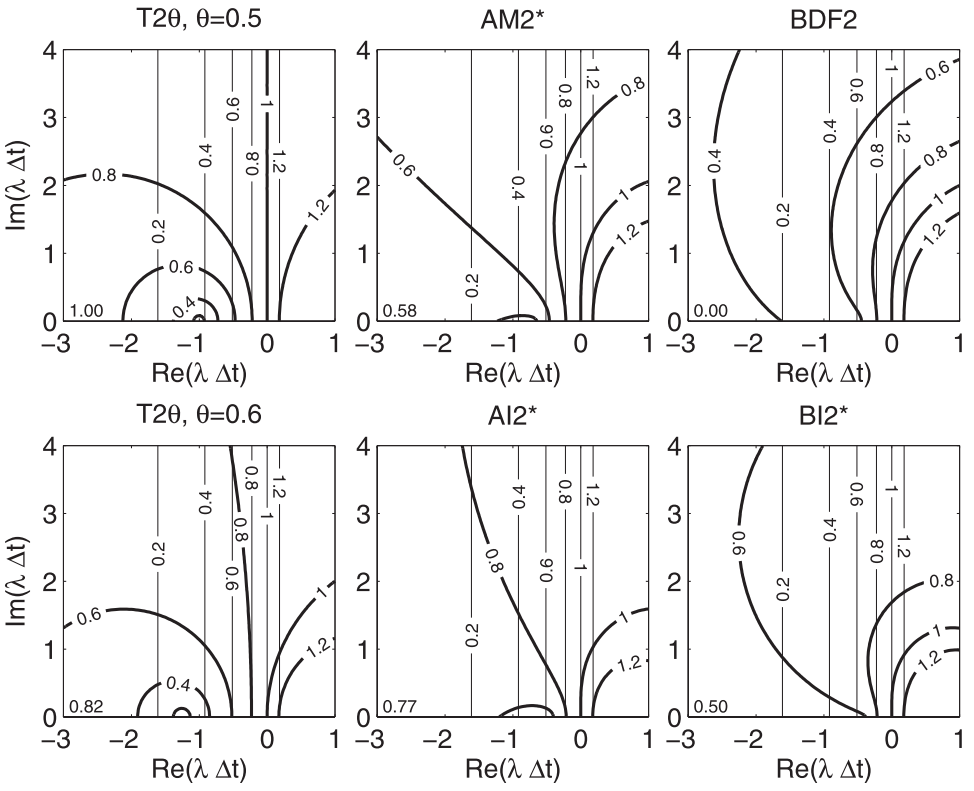


FIG. 1. The magnitude of the amplification factor $|A|$ for several implicit approximations to the test problem in (3), plotted as a function of the real and imaginary parts of $\eta\Delta t$. Also shown, by the thin solid contours, is the magnitude of the amplification factor for the exact solution. The labels correspond to the terminology in the text and Table 1. The number in the bottom left is the limit of $|A|$ as $\Re(\eta) \to -\infty$.

BDF2, they preserve the amplitude of purely oscillatory motions for $|\Im(\eta)\Delta t|$ less than about ½. The exception is the T2$\theta$ method with $\theta = 0.6$, which requires the smallest time step in the purely oscillatory case to avoid spurious damping, yet fails to produce strong damping when $\Re(\eta)\Delta t \to -\infty$.

The damping and phase errors for each of these methods is examined in detail for the purely oscillatory case [$\Re(\eta) = 0$], in Fig. 2. The frequency dependence of the damping is indicated by the plot of $|A|$ as a function of $\Im(\eta)\Delta t$ in Fig. 2a. All the methods preferentially damp the poorly resolved waves, except for T2$\theta$ with $\theta = 0.5$, which correctly preserves the amplitude of the solution. The AM2* method is the second best at preserving the amplitude, the least frequency-selective method is T2$\theta$ with $\theta = 0.6$. The relative phase error

$$R = \frac{1}{\Im(\eta)\Delta t} \arctan\left[\frac{\Im(A)}{\Re(A)}\right],$$

is plotted as a function of $\Im(\eta)\Delta t$ in Fig. 2b; $R$ is the ratio of the phase advance produced by one step of the numerical scheme to the phase advance in the exact solution of (3) over the same time interval. The smallest phase errors are produced by the BDF2 method. AM2* and the T2$\theta$ methods also perform relatively well.[2] The largest phase errors are generated by the AI2* scheme; the BI2* method is the second worst.

### b. The explicit component

When the implicit part of a multistep IMEX scheme is approximated using the modified trapezoidal scheme in (4), the explicit part of the integration is often performed using the leapfrog scheme with Robert–Asselin filtering (Robert 1966; Asselin 1972). Williams (2009, 2011) recently proposed an improvement to this filter, the resulting ''RAW filtered'' leapfrog scheme has the following form:

$$\frac{\mathbf{q}^{n+1} - \tilde{\mathbf{q}}^{n-1}}{2\Delta t} = \mathbf{f}(\tilde{\mathbf{q}}^{n}), \tag{7}$$

[2] T1, the standard trapezoidal method, in which the time difference is computed over an interval of $\Delta t$ rather than $2\Delta t$ as in (4), would give the lowest phase error.

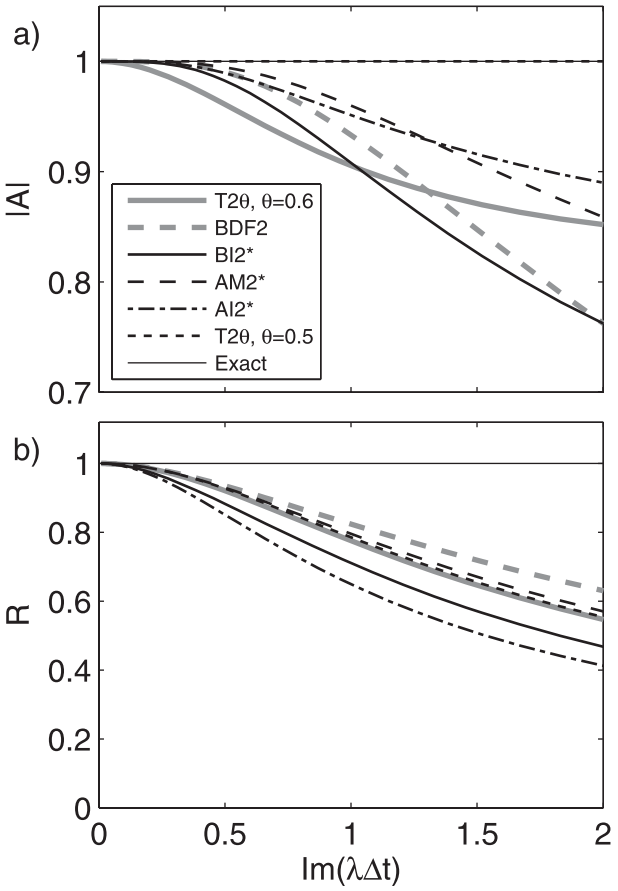


FIG. 2. Magnitude of the (a) amplification factor and (b) relative phase error of the schemes used for the implicit part of the IMEX formulas in Table 1.

$$\tilde{\tilde{\mathbf{q}}}^{n} = \tilde{\mathbf{q}}^{n} + \frac{\sigma\gamma}{2}(\tilde{\tilde{\mathbf{q}}}^{n-1} - 2\tilde{\mathbf{q}}^{n} + \mathbf{q}^{n+1}), \tag{8}$$

$$\tilde{\mathbf{q}}^{n+1} = \mathbf{q}^{n+1} + \frac{(\sigma - 1)\gamma}{2}(\tilde{\tilde{\mathbf{q}}}^{n-1} - 2\tilde{\mathbf{q}}^{n} + \mathbf{q}^{n+1}). \tag{9}$$

Here $\tilde{\mathbf{q}}$ represents a provisional singly filtered value and $\tilde{\tilde{\mathbf{q}}}$ the doubly filtered final value of $\mathbf{q}$, while $\gamma$ and $\sigma$ are constant filter parameters.[3] The original Robert–Asselin formulation (with filter coefficient $\gamma/2$) is obtained by setting $\sigma = 1$. Here we use $\sigma = 0.53$ in the RAW filter following Williams (2009). Depending on the nonlinearity of the underlying problem, time-splitting instability is typically avoided by choosing a value of $\gamma$ in the range $0.05 \leq \gamma/2 \leq 0.2$.

Adams–Bashforth methods are obvious possibilities for the explicit part of multistep IMEX schemes, which use an implicit Adams method. The two-step Adams–Bashforth method is a poor choice because it amplifies oscillatory solutions, but the three-step Adams–Bashforth method (AB3), generally gives good results and is also third-order accurate. As with was the case for implicit Adams methods, for fast-wave–slow-wave IMEX applications, it will be useful to consider the family of three-step methods that are at least second-order accurate. This one-parameter family may be expressed in the following form:

$$\frac{\mathbf{q}^{n+1} - \mathbf{q}^{n}}{\Delta t} = \frac{1}{2}(3 + b)\mathbf{f}(\mathbf{q}^{n}) - \frac{1}{2}(1 + 2b)\mathbf{f}(\mathbf{q}^{n-1}) + \frac{b}{2}\mathbf{f}(\mathbf{q}^{n-2}). \tag{10}$$

The two-step and three-step Adams–Bashforth schemes are obtained by choosing $b = 0$ and $b = 5/6$, respectively.

Suitable explicit methods for use with the implicit backward schemes (6) are less well known. The one-parameter family of three-step explicit backward schemes of at least second-order accuracy has the following form:

$$\frac{\frac{3}{2}\mathbf{q}^{n+1} - 2\mathbf{q}^{n} + \frac{1}{2}\mathbf{q}^{n-1}}{\Delta t} = (2 + b)\mathbf{f}(\mathbf{q}^{n}) - (1 + 2b)\mathbf{f}(\mathbf{q}^{n-1}) + b\mathbf{f}(\mathbf{q}^{n-2}). \tag{11}$$

Choosing $b = 0$ yields a method that has seen use in combination with BDF2 to obtain second-order IMEX methods (Karniadakis et al. 1991; Giraldo et al. 2010).[4] The $b = 0$ method, which we will denote BX2, does have the disadvantage that it erroneously amplifies purely oscillatory solutions. The choice $b = 2/3$ gives a third-order method that will be denoted BX3*; this method is the explicit component of the IMEX BDF2B scheme of Giraldo (2005), who attributed it to Hulsten.

Figure 3 shows $|A|$ for selected explicit methods in the same format as Fig. 1. AX2* and BX2* correspond to the choice $b = 1/2$ in (10) and (11), respectively. The significance of these two schemes will be discussed in the next section. As is well known, the region for which the unfiltered leapfrog scheme generates nongrowing solutions is the segment $(-1, 1)$ along the imaginary axis of the $\Re(\eta)\Delta t - \Im(\eta)\Delta t$ plane. Both the Asselin–Robert and the RAW filter widen this region somewhat, while decreasing the maximum values of $\Im(\eta)\Delta t$ for which $|A| \leq 1$. Nevertheless, the filtered leapfrog schemes remain far less suited to the simulation of damping processes than the other explicit methods shown in Fig. 3. The best scheme for simulating problems with some dissipation is

[3] When the RAW filter is used in leapfrog-trapezoidal IMEX schemes, $\tilde{\tilde{\mathbf{q}}}^{n-1}$ replaces $\mathbf{q}^{n-1}$ in (4).

[4] Varah (1980) and Frank et al. (1997) considered a variant of this method in which the right side is replaced by $\mathbf{f}(2\mathbf{q}^{n} - \mathbf{q}^{n-1})$, which is equivalent to (11) with $b = 0$ when $\mathbf{f}$ is linear.

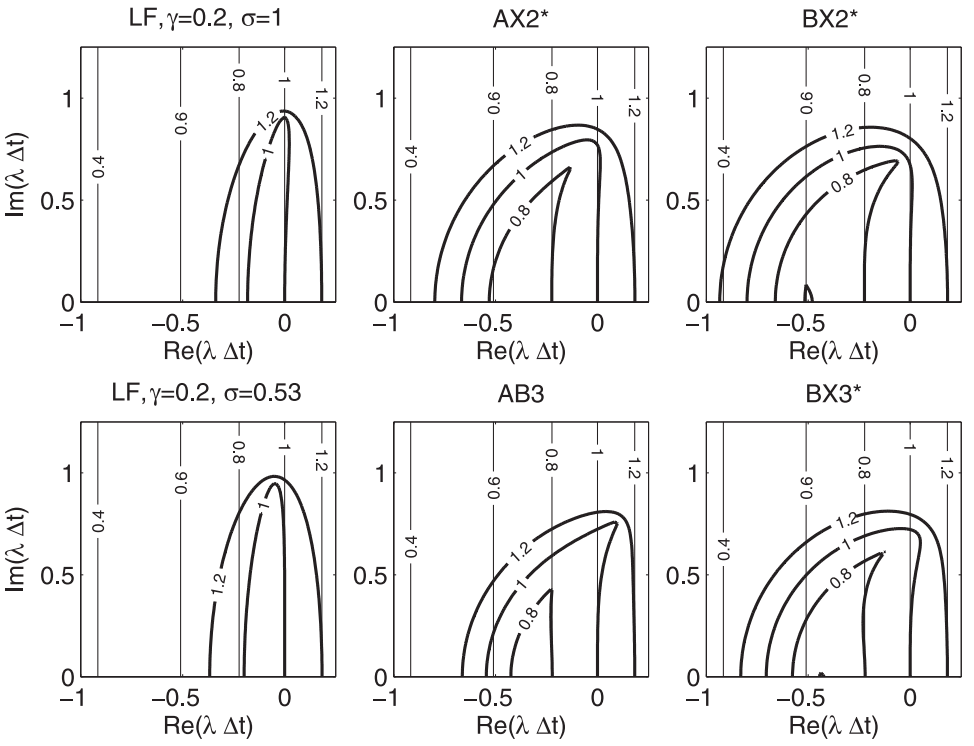


FIG. 3. As in Fig. 1, but for the explicit part of the IMEX formulas in Table 1.

BX2*, which in the $\Im(\eta)\Delta t = 0$ case, does a good job of approximating the correct rate of damping for $-0.5 \leq \Re(\eta)\Delta t \leq 0$ and remains stable for $\Re(\eta)\Delta t$ as negative as roughly $-0.9$.

Further details about the amplification factor for the oscillatory case are shown by the plot of $|A|$ as a function of $\Im(\eta\Delta t)$ in Fig. 4a for the physical mode associated with each of the preceding explicit schemes as well as BX2, which is the previously used version of (11) for which $b = 0$. The unstable amplification generated by BX2 is clearly apparent, as is the weaker damping produced by all other methods except the RAW-filtered leapfrog scheme. The RAW-filtered leapfrog scheme (with $\gamma = 0.2$ and $\sigma = 0.53$) generates very weak damping for $0 \leq \Im(\eta\Delta t) \leq \sim 0.42$, and weak amplification at larger time steps. The stability limits for AB3 and BX3* arise when the amplification factor for one of their two computational modes exceeds unity. Values of $|A|$ for the computational modes associated with the preceding schemes are plotted in Fig. 4b. Among all these methods, AB3 clearly produces the smallest relative phase errors (Fig. 4c).

## 3. Stability analysis of IMEX methods

### a. The oscillation equation

In the preceding section, the properties of the implicit and explicit methods were considered in isolation, but these methods interact in complex ways when combined in an IMEX time integration scheme. For example, despite their attractive properties, the third-order Adams–Bashforth method and trapezoidal method combine to form a IMEX method that is of little use in fast-wave–slow-wave problems (Durran 1991). The stability of IMEX approximations to fast-wave–slow-wave problems can be explored using a variant of the oscillation equation:

$$\frac{\partial q}{\partial t} = i\omega_L q + i\omega_H q, \tag{12}$$

where the frequencies $\omega_H$ and $\omega_L$ represent the oscillations triggered by the propagation of fast and slow waves, respectively.

As an example of the analysis, the implicit–explicit AI2*–AB3 approximation to (12) takes the following form:

$$\frac{q^{n+1} - q^n}{\Delta t} = i\omega_L\left(\frac{23}{12}q^n - \frac{4}{3}q^{n-1} + \frac{5}{12}q^{n-2}\right) + i\omega_H\left(\frac{5}{4}q^{n+1} - q^n + \frac{3}{4}q^{n-1}\right), \tag{13}$$

and the amplification factor $A$ for this method satisfies

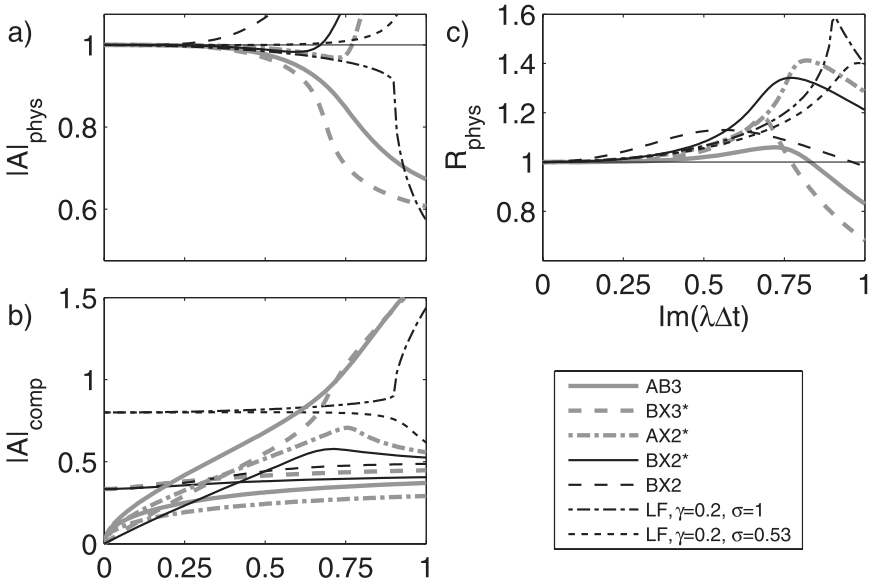


FIG. 4. Magnitude of the (a) amplification factor and (c) relative phase error for the physical modes of the schemes used for the explicit part of the IMEX formulas in Table 1. (b) Magnitudes of the amplification factors for the computational modes.

$$\left(1 - \frac{5}{4}i\omega_H\Delta t\right)A^3 + \left(-1 - \frac{23}{12}i\omega_L\Delta t + i\omega_H\Delta t\right)A^2 + \left(\frac{4}{3}i\omega_L\Delta t - \frac{3}{4}i\omega_H\Delta t\right)A - \frac{5}{12}i\omega_L\Delta t = 0. \quad (14)$$

The amplification factors for the other methods listed in Table 1 were computed in a similar manner. The only complication arises in the analysis of the Asselin-filtered leapfrog scheme, where it is assumed that $\widetilde{A\mathbf{q}} = A\tilde{\mathbf{q}}$ and $\widetilde{A\tilde{\mathbf{q}}} = A\tilde{\tilde{\mathbf{q}}}$ (see Durran 2010, p. 65).

The magnitudes of the amplification factors for several variants of the leapfrog–T2$\theta$ schemes are contoured as a function of $\omega_L\Delta t$ and $\omega_H\Delta t$ in Fig. 5. The result for $\theta = \frac{1}{2}$, $\gamma = 0$ (Fig. 5a) is excellent in the sense that (i) the scheme is stable for all values of $\Delta t$ provided $|\omega_L| < |\omega_H|$ (because $|A| \leq 1$ in the wedge-shaped region $|\omega_L\Delta t| < |\omega_H\Delta t|$), and (ii) even in the case $|\omega_L| > |\omega_H|$, the stability of the method is limited exclusively by the explicitly differenced term (because $|A| \leq 1$ in the vertical strip $|\omega_L\Delta t| < 1$). Off-centering the implicit term by choosing $\theta = 0.6$ (Fig. 5b) preserves stability throughout the wedge-shaped region $|\omega_L\Delta t| < |\omega_H\Delta t|$, but does significantly reduce the range of $\omega_L\Delta t$ over which stable solutions can be obtained when $\omega_H\Delta t$ is small—a counterintuitive result since off-centering the trapezoidal method adds damping that one would think might increase stability.

As mentioned previously, a serious difficulty with the pure leapfrog scheme is that, in nonlinear problems, the solution may be subject to time-splitting instability. When $\theta = 0.5$, using the RA filter [$\sigma = 1$ in (8)–(9)] with $\gamma = 0.2$, produces only a modest influence on the geometry of the stable region for small values of $\omega_H\Delta t$, but does restrict the stability condition for larger time steps, since $|\omega_L| < 1.22|\omega_H|$ becomes the corresponding stability condition for arbitrary $\Delta t$ (cf. Figs. 5a,c). A similar modest reduction in stability is produced by increasing $\gamma$ from 0 to 0.2 if the implicit scheme is off-centered with $\theta = 0.6$ (cf. Figs. 5b,d). The stability condition $|\omega_L\Delta t| < |\omega_H\Delta t|$ is recovered when the new RAW filter is used (with $\sigma = 0.53$ and $\gamma = 0.2$) instead of the RA filter, but there is a reduction in stability when $\omega_H\Delta t$ is small (for both $\theta$ values).

Two parameters describing simple aspects of the stability region for the T2$\theta$–LF scheme are listed in Table 2: $\mu$ characterizes the stability when no high-frequency oscillation is present in the sense that stability is guaranteed if $|\omega_L\Delta t| < \mu$ and $|\omega_H\Delta t| = \epsilon$, where $\epsilon > 0$ is an arbitrarily small constant.[5] In contrast, $\xi$ is the smallest value for which stable solutions may be obtained regardless of the value $\Delta t$ provided $|\omega_L| < \xi|\omega_H|$; as such, it characterizes the spread of the widest wedge-shaped subset of the region of unconditional stability emanating upward from the origin.

The magnitudes of the amplification factors for the other methods listed in Table 1, are shown in Fig. 6,[6] and

[5] The case $\epsilon = 0$ is not included because for many schemes that are unstable arbitrarily close to the origin, $|A| \to 1$ as $|\omega_H\Delta t| \to 0$.

[6] Discussion of the MCN/AX2+ scheme, listed in Table 1, will be deferred until the conclusions.

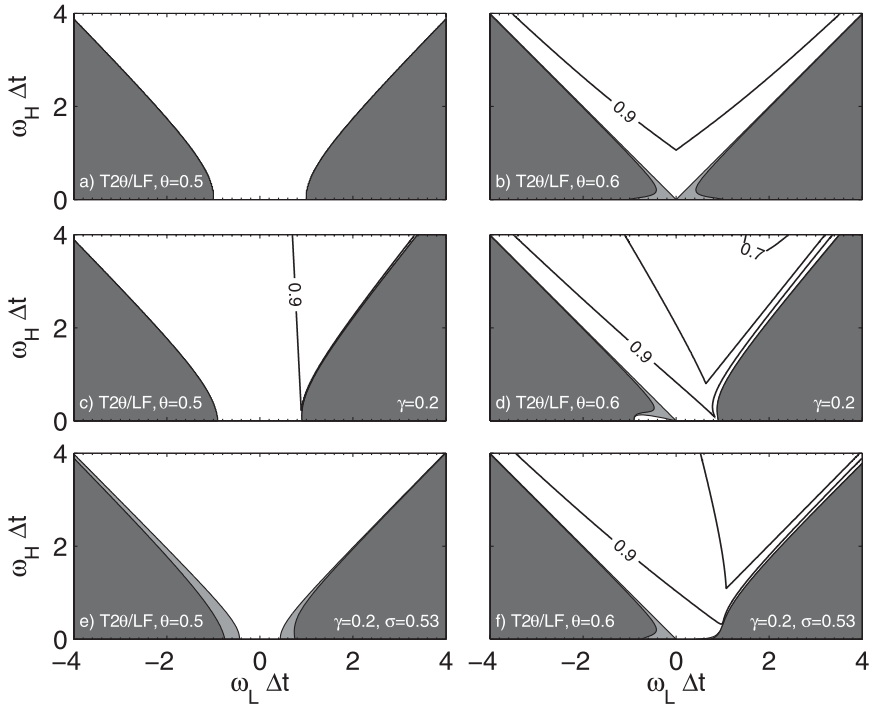


FIG. 5. Magnitude of the amplification factor for the leapfrog-based IMEX schemes listed in Table 2 for the model problem (12). The contour interval is 0.1, but regions with $1 < |A| < 1.01$ are shaded gray and regions in which $|A|$ exceeds 1.01 are shaded dark gray. Only the upper half-plane is plotted, the values of $|A|$ in the lower half plane are antisymmetric about the origin.

the values of $\mu$ and $\xi$ for these methods are also listed in Table 2. The T1–AB3 combination (Fig. 6a) has a very small region of stability, and as noted in Durran (1991), is not suitable for fast-wave–slow-wave problems. In particular, $\mu = 0$ and $\xi = \infty$ for the T1–AB3 scheme. The previously used combination BDF2–BX2 (Fig. 6b) requires the frequency of the fast oscillation to dominate that of the slow oscillation by the factor of $\xi = 3$, which is considerably worse than the values of $\xi$ for the leapfrog-trapezoidal-based methods, but not worse than that for some of the other schemes shown in Fig. 6. The stability of the BDF2–BX2 method is, however, poor in the case where $|\omega_H \Delta t|$ is small, indeed $\mu = 0$ for this method.

Near the origin in the $\omega_L \Delta t - \omega_H \Delta t$ plane, the geometry of the regions of instability in IMEX multistep methods often includes the line $\omega_H \Delta t = -\omega_L \Delta t$ (as in Figs. 5d and 6a,b). In addition, the region of stability along the line $\omega_H \Delta t = 0$ can also be quite limited. We therefore conducted an empirical search for those combinations of IMEX Adams schemes and those combinations of IMEX backward schemes that were stable along the piecewise linear curve:

$$\omega_H \Delta t = 1/2 - |\omega_L \Delta t|, \quad \omega_L \Delta t \in [-1/2, 1/2]. \quad (15)$$

This curve is indicated by the heavy black line in each panel of Fig. 6.

The criteria for stable IMEX schemes along this segment proved surprisingly simple. IMEX Adams schemes, formed by combining (5) and (10), give stable

TABLE 2. Parameters characterizing regions of stability for solutions to (12) using the implicit–explicit multistep methods listed in Table 1. Values for LF–RA were computed using $\gamma = 0.2$, $\sigma = 1$, while for the LF–RAW variant, $\gamma = 0.2$, $\sigma = 0.53$.

| Method | | | | |
|---|---|---|---|---|
| Implicit | Explicit | $\theta$ | $\mu$ | $\xi$ |
| T2$\theta$ | LF | 0.5 | 1 | 1 |
| T2$\theta$ | LF | 0.6 | 0 | 1 |
| T2$\theta$ | LF–RA | 0.5 | 0.91 | 1.22 |
| T2$\theta$ | LF–RA | 0.6 | 0 | 1.17 |
| T2$\theta$ | LF–RAW | 0.5 | 0.43 | 1.02 |
| T2$\theta$ | LF–RAW | 0.6 | 0 | 1 |
| T1 | AB3 | — | 0 | $\infty$ |
| AM2* | AX2* | — | 0.76 | 3 |
| AI2* | AB3 | — | 0.72 | 1.23 |
| BDF2 | BX2 | — | 0 | 3 |
| BDF2 | BX2* | — | 0.67 | 5 |
| BI2* | BX3* | — | 0.72 | 2.43 |

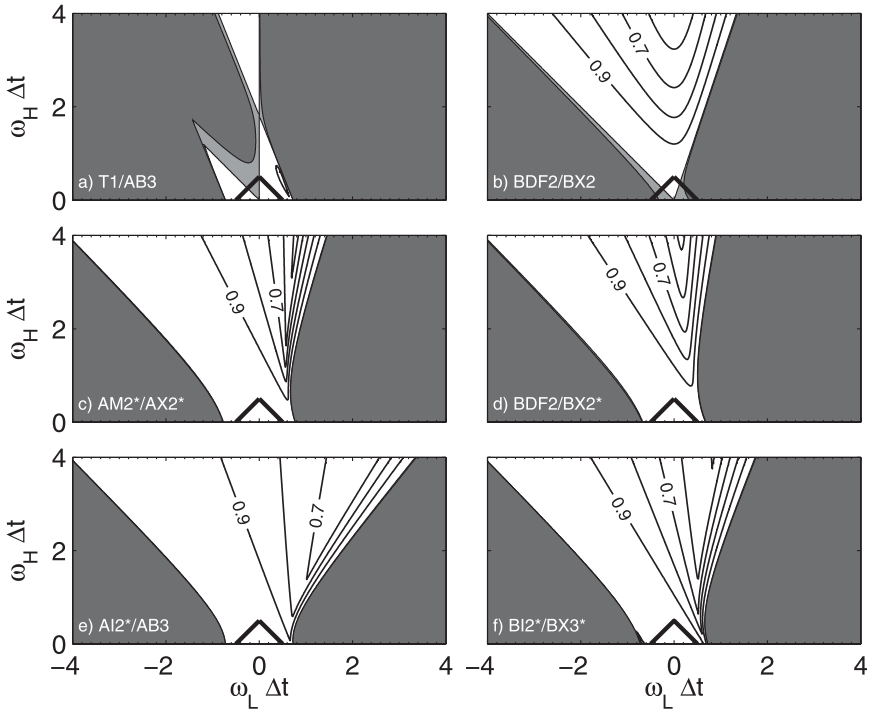


FIG. 6. As in Fig. 5, but for the Adams and the backward-differenced IMEX schemes listed in Table 1.

approximations to (12) for all ($\omega_L \Delta t$, $\omega_H \Delta t$) along (15) provided $b$ and $c$ satisfy

$$c = 3b + 1, \quad 0.105 < c < 3.85. \tag{16}$$

We do not have an analytic proof that this is the optimal relation between $b$ and $c$, but it does seem likely that the coefficients defining the relation are actually the preceding integers. If the intercept in (15) was perturbed by just $\pm 0.01$ it was not possible to find any values of $b$ or $c$ for which the resulting IMEX Adams method was stable for all points along the segment in (15). In a similar way, the optimal combination of backward schemes in (6) and (11) was empirically determined to be

$$c = 2b + 1, \quad -0.158 < c < 2.00. \tag{17}$$

Once again, this result is robust to perturbation of the intercept by values of $\pm 0.01$ and larger.

What criteria might we use to choose among the members of these one-parameter families of stable Adams and backward IMEX methods for fast-wave–slow-wave problems? In cases where the fast wave is low amplitude and of essentially no physical significance (e.g., sound waves), the best accuracy can often be obtained using the value of $b$ associated with the third-order explicit scheme. This yields the methods AI2*–AB3 and BI2*–BX3* shown in Figs. 6e,f. In comparison with the other methods shown in Fig. 6, both of these methods have relatively large stability regions. In particular, the AI2*–AB3 scheme is unconditionally stable throughout the relatively wide wedge defined by $\xi = 1.23$. Furthermore, like the centered ($\theta = 0.5$) variant of the T2$\theta$–LF scheme, whenever $|\omega_L| > |\omega_H|$ the stability of AI2*–AB3 combination is limited exclusively by the explicitly differenced term (i.e., $\mu = 0.72$).

Alternatively, if an accurate treatment of the implicitly approximated terms is important, which may be the case when most of the terms fundamental to gravity wave propagation are treated implicitly, it can be advantageous to choose the most accurate implicit scheme available, and then select a compatible explicit method using (16) or (17). For Adams methods, following Nevanlinna and Liniger (1978), we propose AM2* as the implicit scheme, and for the implicit backward method we use classic $L$-stable BDF2. Among the schemes plotted in Fig. 2, BDF2 and AM2* produce the smallest phase errors, while the largest errors are produced by BI2* and AI2*. In addition, the amplitude errors generated by AM2* are smaller than those from AI2*, and those created by BDF2 are smaller than the ones from BI2*. The stability regions for the resulting combinations, AM2*–AI2* and BDF2–BX2* are shown in Figs. 6c,d, respectively. Values of $\mu$ and $\xi$ for all these schemes are also given in Table 2.

*b. The Euler equations*

The oscillation equation provides a simple prototype problem that is helpful for assessing the basic behavior of IMEX methods. In practical applications, many waves may be present, they may move at a variety of different speeds, and several processes may be responsible for propagating each individual wave. To examine the behavior of the IMEX mulitstep methods in a more realistic fluid dynamical context, consider the linearized two-dimensional ''compressible Boussinesq system'' (Durran 2010, p. 409):

$$\left(\frac{\partial}{\partial t} + U\frac{\partial}{\partial x}\right)u + \underbrace{\frac{\partial P}{\partial x}}_{\text{s}} = 0, \tag{18}$$

$$\left(\frac{\partial}{\partial t} + U\frac{\partial}{\partial x}\right)w + \underbrace{\frac{\partial P}{\partial z}}_{\text{s}} = \underbrace{b}_{\text{b}}, \tag{19}$$

$$\left(\frac{\partial}{\partial t} + U\frac{\partial}{\partial x}\right)b + \underbrace{N^2 w}_{\text{b}} = 0, \tag{20}$$

$$\left(\frac{\partial}{\partial t} + U\frac{\partial}{\partial x}\right)P + \underbrace{c_s^2\left(\frac{\partial u}{\partial x} + \frac{\partial w}{\partial z}\right)}_{\text{s}} = 0. \tag{21}$$

Here $U$ is the constant mean horizontal wind speed; $u$ and $w$ are the perturbation horizontal and vertical wind speeds, respectively; and $c_s$ is the speed of sound. The reference-state pressure $\overline{p}(z)$ is assumed to be in hydrostatic balance with the reference-state density $\overline{\rho}(z)$, and the buoyancy $b$, Boussinesq pressure potential $P$, and Brunt–Väisälä frequency $N$ are defined such that

$$b = -g\frac{\rho - \overline{\rho}(z)}{\rho_0}, \quad P = \frac{p - \overline{p}(z)}{\rho_0}, \quad N^2 = -\frac{g}{\rho_0}\frac{d\overline{\rho}}{dz}, \tag{22}$$

where $\rho_0$ is constant representative value for the density.

Let $(u_0, w_0, b_0, P_0)$ be complex valued amplitudes for the prognostic variables $(u, w, b, P)$. Then wavelike solutions to (18)–(21) of the following form:

$$\Re[(u_0, w_0, b_0, P_0)e^{i(kx+lz-\omega t)}] \tag{23}$$

exist provided $k$ and $l$, the wavenumbers in the $x$ and $z$ directions, and $\omega$, the frequency, satisfy the dispersion relation:

$$(\omega - Uk)^2 = \frac{c_s^2}{2}\left\{k^2 + \ell^2 + \frac{N^2}{c_s^2} \pm \left[\left(k^2 + \ell^2 + \frac{N^2}{c_s^2}\right)^2 - \frac{4N^2k^2}{c_s^2}\right]^{1/2}\right\}. \tag{24}$$

The positive root in (24) is associated with sound waves, which remain nontrivial solutions in the limit $N \to 0$. The pressure-gradient and divergence terms fundamental to sound wave propagation are indicated by underbraces labeled ''s'' in (18), (19), and (21). The negative root in (24) is associated with gravity (or buoyancy) waves. The forces fundamental to gravity wave propagation again include pressure gradient forces, as well as the processes involving buoyancy indicated by the terms with underbraces labeled ''b'' in (19) and (20). Both sound and gravity waves are also transported by the mean wind through advection, which is represented by the terms involving the factor $U$ in (18)–(21).

In atmospheric applications,[7] $N^2/c_s^2 \ll l^2$ and, as discussed in Durran (2010, p. 412) the frequencies corresponding to gravity waves in (24) are well approximated by the following relation:

$$\omega = Uk \pm \frac{Nk}{(k^2 + l^2 + N^2/c_s^2)^{1/2}}. \tag{25}$$

The frequency increases as the vertical wavelength increases ($l \to 0$) or the horizontal wavelength decreases ($k \to \infty$), and is bounded by $|Uk_{\max}| + N$, where $k_{\max}$ is the maximum horizontal wavenumber (corresponding to the shortest horizontal wavelength) retained on the spatial mesh. A sufficient condition for the stability of the gravity wave modes in a *completely explicit* approximation typically takes the following form:

$$(|Uk_{\max}| + N)\Delta t < C, \tag{26}$$

where $C$ is a constant of order unity whose precise value depends on the numerical integrator. For the leapfrog scheme without time filtering, $C = 1$; for AB3, $C = 0.72$ and for BX2* $C = 0.67$.

Under the same approximation that $N^2/c_s^2 \ll l^2$, the frequencies for the sound waves are well approximated as

$$\omega^2 = c_s^2(k^2 + \ell^2 + N^2/c_s^2). \tag{27}$$

[7] For example, if $N = 0.01\ \text{s}^{-1}$ and $c_s = 300\ \text{m s}^{-1}$, $N^2/c_s^2$ can be neglected in comparison with $l^2$ unless the vertical wavelength exceeds 100 km.

Letting $\kappa^2 = k^2 + l^2$ and again neglecting the term $N^2/c_s^2$, the stability condition for the sound wave modes in a completely explicit approximation typically takes the following form:

$$c_s \kappa_{\max} \Delta t < C, \tag{28}$$

where $\kappa_{\max}$ is the maximum total wavenumber (associated with the shortest wavelength) retained on the spatial mesh, and $C$ is again a constant dependent on the numerical integrator. For the pure leapfrog scheme, AB3, and BX2*, $C$ takes the same specific values previously mentioned in connection with (26). The stability restriction for the sound waves (28) is typically much more severe than that for the gravity waves in (26), because the vertical resolution in atmospheric models is typically much finer than the horizontal resolution and $c_s$ is large.

To allow a larger time step than that required to stabilize the sound waves, first consider IMEX approximations to (18)–(21) in which the terms labeled "s" are treated implicitly, and all the remaining terms are stepped forward with an explicit scheme. The quantities defined in (1) become

$$\mathbf{u} = \begin{pmatrix} u \\ w \\ b \\ P \end{pmatrix}, \quad \mathbf{f}(\mathbf{u}) = \begin{pmatrix} -U\dfrac{\partial u}{\partial x} \\ -U\dfrac{\partial w}{\partial x} + b \\ -U\dfrac{\partial b}{\partial x} - N^2 w \\ -U\dfrac{\partial P}{\partial x} \end{pmatrix},$$

$$L\mathbf{u} = \begin{bmatrix} -\dfrac{\partial P}{\partial x} \\ -\dfrac{\partial P}{\partial z} \\ 0 \\ -c_s^2\left(\dfrac{\partial u}{\partial x} + \dfrac{\partial w}{\partial z}\right) \end{bmatrix}. \tag{29}$$

Having linearized the governing equations, $\mathbf{f}(\mathbf{u})$ is no longer a nonlinear function of $\mathbf{u}$, and we will alternatively write this term as $\mathbf{Mu}$.

If (29) is integrated using the AI2*–AB3 method, the temporally discretized system becomes

$$\mathbf{P}_3\mathbf{u}^{n+1} + \mathbf{P}_2\mathbf{u}^{n} + \mathbf{P}_1\mathbf{u}^{n-1} + \mathbf{P}_0\mathbf{u}^{n-2} = \mathbf{0}, \tag{30}$$

where each of the $\mathbf{P}_n$ are $4 \times 4$ matrices, with $\mathbf{P}_3 = \mathbf{I} - (5/4)\mathbf{L}\Delta t$, $\mathbf{P}_2 = -\mathbf{I} - (23/12)\mathbf{M}\Delta t + \mathbf{L}\Delta t$, $\mathbf{P}_1 = (4/3)\mathbf{M}\Delta t - (3/4)\mathbf{L}\Delta t$, and $\mathbf{P}_0 = -(5/12)\mathbf{M}\Delta t$. The method in (30) supports four physical modes [two sound wave and two gravity wave modes that are the discrete-in-time equivalents of (23)] and eight computational modes, all of which are eigenvectors associated with the polynomial eigenvalue problem:

$$(\lambda^3\mathbf{P}_3 + \lambda^2\mathbf{P}_2 + \lambda\mathbf{P}_1 + \mathbf{P}_0)\mathbf{u}^{n-2} = \mathbf{0}. \tag{31}$$

Note that (31) is the matrix analog of (14) with the amplification factor $A$ replaced by the eigenvalue $\lambda$. Such polynomial eigenvalue problems can be solved in MATLAB using the command polyeig or, when $\mathbf{P}_3$ is nonsingular, by reformulating (31) as the standard eigenvalue problem $\mathbf{Bv} = \lambda\mathbf{v}$ where

$$\mathbf{B} = \begin{pmatrix} \mathbf{P}_3^{-1}\mathbf{P}_2 & \mathbf{P}_3^{-1}\mathbf{P}_1 & \mathbf{P}_3^{-1}\mathbf{P}_0 \\ \mathbf{I} & 0 & 0 \\ 0 & \mathbf{I} & 0 \end{pmatrix} \quad \text{and} \quad \mathbf{v} = \begin{pmatrix} \mathbf{u}^n \\ \mathbf{u}^{n-1} \\ \mathbf{u}^{n-2} \end{pmatrix}. \tag{32}$$

The latter approach was taken for the computations in this paper.

Let $\Psi$ be the maximum in absolute value of the eigenvalues arising from such a discrete-in-time IMEX approximation. Figure 7 shows $\Psi$ for the T2$\theta$–LF,[8] AI2*–AB3, and BDF2–BX2* methods. Key values of $\Psi$ are contoured as a function of $\Delta t$ and the horizontal wavelength $\lambda_x = 2\pi/k$ for modes with fixed vertical wavelengths $\lambda_z = 2\pi/l$ of either 20 or 2 km. As apparent in Fig. 7, if $\Delta t$ is increased, a mode with given $(\lambda_x, \lambda_z)$ eventually exhibits spurious amplification, although the $\Delta t$ at which this first occurs are not captured for all the horizontal wavelengths plotted in Figs. 7d,e. Also plotted as the solid line is the curve $F_1(\lambda_x, \Delta t) = C$, where $F_1 = (|2\pi U/\lambda_x| + N)\Delta t$ and $C$ is 1.0, 0.72, or 0.67 for the T2$\theta$–LF, AI2*–AB3, and BDF2–BX2* methods, respectively. Note that $F_1(\lambda_x, \Delta t)$ is similar to the expression appearing in the stability condition in (26) except that it is expressed in terms of the actual wavelength $\lambda_x$ instead of the maximum resolved wavenumber $k_{\max}$. The curve $F_1(\lambda_x, \Delta t) = C$ divides the stable and unstable regions in the T2$\theta$–LF case, but lies within the stable region for the AI2*–AB3 and BDF2–BX2* cases.

The dashed curve in Fig. 7 shows the limit of the stability region for explicit LF, AB3, or BX2* approximations to the highest-frequency gravity wave mode with horizontal and vertical wavelengths $(\lambda_x, \lambda_z)$, that is, the dashed curve plots $F_2(\lambda_x, \Delta t) = C$, where $F_2(\lambda_x, \Delta t) = \omega_{\mathrm{gD}}\Delta t$, $\omega_{\mathrm{gD}}$ is the frequency determined by (25) for the downstream-propagating mode, and $C$ is 1.0, 0.72 or 0.67 in the respective T2$\theta$–LF, AI2*–AB3, and BDF2–BX2*

[8] Throughout the following analysis of the T2$\theta$–LF scheme, we assume $\theta = 0.5$ and no time filtering.

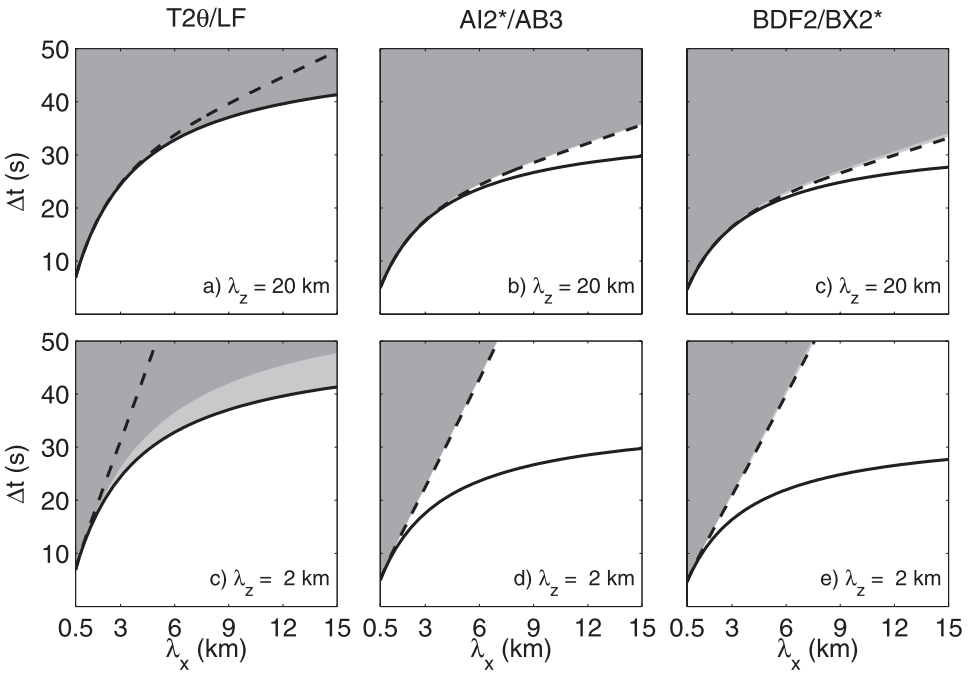


FIG. 7. Stable regions as determined from the maximum eigenvalue $\Psi$ for wave solutions to the compressible Boussinesq equations using the IMEX decomposition in (29). The quantity $\Psi$ is contoured as function of horizontal wavelength and time step for modes with vertical wavelengths of (top) 20 and (bottom) 2 km. Values in columns (left to right) for the T2$\theta$–LF, AI2*–AB3, and BDF2–BX2* methods. Regions with $0 \leq \Psi \leq 1$ are white, those with $1 < \Psi < 1.01$ are light gray, and regions in which $\Psi$ exceeds 1.01 are dark gray. Also plotted are the curves for $F_1(\lambda_x, \Delta t) = C$ (solid line) and $F_2(\lambda_x, \Delta t) = C$ (dashed); see text.

cases. Since this curve matches the edge of the stable region in the AI2*–AB3 and BDF2–BX2* cases, both of these methods are stable whenever the associated explicit approximation (AB3 or BX2*) to the same gravity wave mode would be stable. In contrast, the region of stability for the T2$\theta$–LF method is more restrictive than that for leapfrog approximations to the same gravity wave mode.[9] The maximum stable time step for a mode of wavenumber $k$ is reduced for the T2$\theta$–LF method relative to that for gravity waves of wavenumber $k$ integrated with a fully explicit leapfrog scheme because the $2\Delta t$-trapezoidal averaging in the implicit step replaces $c_s$ in (24) with $\hat{c}_s = c_s \cos(\omega \Delta t)$. As $\omega \Delta t$ increases toward $\pi/2$ (a coarsely resolved $4\Delta t$ oscillation), the terms involving $N^2/\hat{c}_s^2$ begin to dominate the semidiscrete dispersion relation for the *sound wave* modes. In the limit $\hat{c}_s \to 0$, that dispersion relation becomes

$$\left[\frac{\sin(\omega \Delta t)}{\Delta t} - Uk\right]^2 = \frac{\hat{c}_s^2}{2}\left(\frac{N^2}{\hat{c}_s^2} + \frac{N^2}{\hat{c}_s^2}\right) = N^2,$$

from which it follows that the condition $(Uk + N)\Delta t < 1$ is not only sufficient, but is also necessary for stability.

It is interesting that the implicitness introduced in the AI2*–AB3 and the BDF2–BX2* schemes avoids the negative impact on the stability of individual gravity wave modes, relative to the corresponding fully explicit approach, produced by the T2$\theta$–LF method. Nevertheless, the maximum $\Delta t$ in any practical IMEX integration of (29) is limited by the numerically resolvable mode with the most severe stability constraint, and as apparent in Fig. 7, these are the modes with the shortest horizontal wavelengths. The maximum $\Delta t$ is effectively limited by the stability condition in (26), and the largest time step allowed by the AI2*–AB3 (BDF2–BX2*) scheme is therefore smaller than that for the T2$\theta$/LF method by a factor of 0.72 (0.67).

If the horizontal resolution is sufficiently coarse, $|Uk_{\max}| \ll N$ and (26) reduces to

$$N\Delta t < C, \tag{33}$$

in which case the time step is determined entirely by the Brunt–Väisälä frequency. In atmospheric applications, the maximum $N$ is $O(10^{-2})$ s$^{-1}$ and the maximum stable time step dictated by (33) will be less than roughly 100 s. This time-step restriction can be relaxed

[9] Of course completely explicit AB3 and leapfrog approximations to (18)–(21) would face more severe stability restrictions on $\Delta t$ from the sound waves.

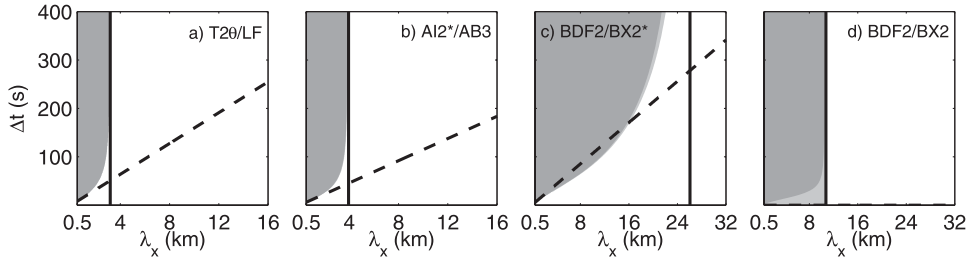


FIG. 8. (a)–(d) Contours of $\Psi$ indicating stable regions as in the first row of Fig. 7, but for the IMEX decomposition (34), and (d) the addition of the BDF2–BX2 method. Shading convections are as in Fig. 7. Note the horizontal scale in (c),(d) is almost double that in (a),(b). Also shown are the lines $\tilde{\omega}_L \Delta t = C$ (dashed) and $\tilde{\omega}_H/\tilde{\omega}_L = \xi$ (solid).

by treating the terms labeled b in (19) and (20) implicitly, in which case an IMEX splitting of the form (1) becomes

$$\mathbf{f}(\mathbf{u}) = \begin{pmatrix} -U\dfrac{\partial u}{\partial x} \\ -U\dfrac{\partial w}{\partial x} \\ -U\dfrac{\partial b}{\partial x} \\ -U\dfrac{\partial P}{\partial x} \end{pmatrix}, \quad L\mathbf{u} = \begin{bmatrix} -\dfrac{\partial P}{\partial x} \\ -\dfrac{\partial P}{\partial z} + b \\ -N^2 w \\ -c_s^2\left(\dfrac{\partial u}{\partial x} + \dfrac{\partial w}{\partial z}\right) \end{bmatrix}. \quad (34)$$

The implicit part of (34) includes all the terms responsible for gravity wave propagation in a resting fluid; if the vertical wavelength is sufficiently long, this propagation will be faster than that produced by typical atmospheric mean flows. Let us, therefore, denote the frequencies due to the gravity wave propagation as $\tilde{\omega}_H$ and that due to advection as $\tilde{\omega}_L$, where for a specific mode

$$\tilde{\omega}_L = |Uk|, \quad \tilde{\omega}_H = \frac{N|k|}{(k^2 + l^2)^{1/2}}.$$

Figure 8 shows $\Psi$ for T2$\theta$–LF, AI2*–AB3, BDF2–BX2*, and BDF2–BX2 approximations to (34) contoured as a function of $\lambda_x$ and $\Delta t$ for the downstream-moving gravity wave with a vertical wavelength of 20 km. Noting the difference in the scales on the vertical axis between Figs. 7 and 8, it is apparent that when $\lambda_x$ is large, stable solutions to (34) can be obtained using much larger $\Delta t$ than would be permitted when integrating the same mode using (29). To better appreciate the factors governing the stability of IMEX solutions to (34), two additional lines are plotted in Fig. 8. First consider the line $\tilde{\omega}_L \Delta t = C$ (dashed), where as before $C$ is 1.0, 0.72, and 0.67 for the T2$\theta$–LF, AI2*–AB3, and BDF2–BX2* approximations, respectively.[10] This line approximates the stability boundary for both schemes when the horizontal wavelength is short and the intrinsic frequency of the gravity waves are reduced by nonhydrostatic effects. These values are consistent with the values of $\omega_L \Delta t$ at which the stability boundary intersects the horizontal axis in Figs. 5a and 6d,e. Also consistent with Fig. 6b is the lack of a significant stable region for small horizontal wavelengths in the BDF2/BX2 case (Fig. 8d). Now consider the vertical line in each panel of Fig. 8, which is plotted at the value of $\lambda_x$ for which $\tilde{\omega}_H/\tilde{\omega}_L = \xi$. The region to the right of this line is the region where the intrinsic frequency of the gravity waves exceeds that frequency produced by advection by a large enough factor to guarantee stability, independent of the value of $\Delta t$, and consistent with Table 2, this is indeed the case.

## 4. A nonlinear test case

The preceding theoretical analyses suggest new methods that may be attractive candidates for IMEX approximations to the compressible equations of motion. In this section we evaluate the performance of several of these methods in a pair of nonlinear test cases involving two-dimensional ($x$–$z$) nonlinear gravity waves generated by a localized region of nondivergent forcing in a stratified shear flow. The background horizontal wind is

$$u_0(z) = 5 + z + 0.4(5 - z)(5 + z) \text{ m s}^{-1},$$

where $z$ is the vertical coordinate in kilometers. The waves are forced by the curl of a nondivergent streamfunction:

$$\psi(x, z, t) = \psi_0\left(\frac{\pi x}{L_x}\right) \sin(\omega t) \exp\left[-\left(\frac{\pi x}{L_x}\right)^2 - \left(\frac{\pi z}{L_z}\right)^2\right] \text{m}^2 \text{ s}^{-1},$$

[10] This line does not appear in Fig. 8d.

TABLE 3. Physical and numerical parameters for the nonlinear simulations.

| Parameter | Case NH | Case H |
|---|---|---|
| Physical parameters | | |
| $\omega$ ($s^{-1}$) | 0.005 | $1.25 \times 10^{-4}$ |
| $L_x$ (km) | 20 | 160 |
| $L_z$ (km) | 5 | 10 |
| $\psi_0$ ($m^2\ s^{-1}$) | 4 | 10 |
| Numerical parameters | | |
| Domain width (km) | 300 | 12,000 |
| Domain depth (km) | 10 | 10 |
| $\Delta x$ (km) | 0.25 | 10 |
| $\Delta z$ (m) | 50 | 250 |
| $K$ ($s^{-1}$) | $4.69 \times 10^{-4}$ | $1.17 \times 10^{-5}$ |
| Diagnosis time $t_d$ (s) | 3000 | $1.2 \times 10^5$ |
| End time $t_f$ (s) | $10^5$ | $4 \times 10^6$ |

where $x$ denotes the horizontal coordinate in kilometers, and the values of $\psi_0$, $\omega$, $L_x$, and $L_z$ for each case are listed in Table 3.

The first case, NH for which $\omega/N = 1/4$, is dominated by nonhydrostatic motions and employs a grid spacing representative of high-resolution convective cloud models (see Table 3 for values of the numerical parameters). The dynamics in the second case, H for which $\omega/N = 6.25 \times 10^{-3}$, are quasi-hydrostatic and the grid spacing in this case is representative of a high-resolution global model. Empirical stability limits for the various methods are determined by integrating each scheme to a time $t_f$, chosen such that, at the coarsest time resolution, more than 8500 time steps are required to reach $t_f$. In case NH, the waves generated by the forcing break in very localized regions and gradually accelerate the mean flow. To keep the effective Courant–Friedrichs–Lewy (CFL) number constant during the longtime NH integrations, the horizontally averaged mean flow $\overline{u}$ is gradually relaxed back toward its initial shear profile over a time scale $\tau = 3000$ s. No relaxation is used in case H.

This problem is governed by the following system:

$$\frac{Du}{Dt} + \frac{\partial P}{\partial x} = -\frac{\partial \psi}{\partial z} + \frac{u_0(z) - \overline{u}(z,t)}{\tau}, \tag{35}$$

$$\frac{Dw}{Dt} + \frac{\partial P}{\partial z} = b + \frac{\partial \psi}{\partial x}, \tag{36}$$

$$\frac{Db}{Dt} + N^2 w = 0, \tag{37}$$

$$\frac{DP}{Dt} + c_s^2\left(\frac{\partial u}{\partial x} + \frac{\partial w}{\partial z}\right) = 0, \tag{38}$$

where

$$\frac{D}{Dt} = \frac{\partial}{\partial t} + u\frac{\partial}{\partial x} + w\frac{\partial}{\partial z},$$

$N = 0.02\ s^{-1}$ and $c_s = 350\ m\ s^{-1}$.

We will investigate convergence in the time domain while keeping the spatial discretization fixed. In all simulations the numerical domain is horizontally periodic and bounded by flat rigid upper and lower surfaces. Let $m$ and $n$ be integer indices; the mesh is staggered so that the equation for $P$ applies at points $(m\Delta x, n\Delta y)$, that for $u$ applies at points $\{[m - (1/2)]\Delta x, n\Delta z\}$, and those for $b$ and $w$ at points $\{m\Delta x, [n - (1/2)]\Delta z\}$. Using the following operator notation:

$$\delta_{nx} f(x) = \frac{f(x + n\Delta x/2) - f(x - n\Delta x/2)}{n\Delta x},$$

$$\langle f(x)\rangle^{nx} = \frac{f(x + n\Delta x/2) + f(x - n\Delta x/2)}{2},$$

the spatial finite differencing has the following form:

$$\frac{\partial u}{\partial t} + \frac{1}{2}\delta_{2x}(u^2) + \langle\langle w\rangle^x \delta_z u\rangle^z + \delta_x P = \frac{u_0(z) - \overline{u}(z,t)}{\tau} - K[(\Delta x\delta_x)^2 + (\Delta z\delta_z)^2]^2 u, \tag{39}$$

$$\frac{\partial w}{\partial t} + \langle\langle u\rangle^z \delta_x w\rangle^x + \frac{1}{2}\delta_{2z}(w^2) + \delta_z P - b = -K[(\Delta x\delta_x)^2 + (\Delta z\delta_z)^2]^2 w, \tag{40}$$

$$\frac{\partial b}{\partial t} + \langle\langle u\rangle^z \delta_x b\rangle^x + \langle\langle w\rangle^z \delta_z b\rangle^z + N^2 w = -K[(\Delta x\delta_x)^2 + (\Delta z\delta_z)^2]^2 b, \tag{41}$$

$$\frac{\partial P}{\partial t} + \langle u\delta_x P\rangle^x + \langle w\delta_z P\rangle^z + c_s^2(\delta_x u + \delta_z w) = 0, \tag{42}$$

where nonlinear instability is prevented and a simple parameterization of turbulent mixing in a nearly inviscid fluid is imposed through the fourth-derivative hyperdiffusion terms with the values of $K$ listed in Table 3. The pressure field for the T2$\theta$–LF scheme is updated solving a Helmholtz equation for pressure in the manner described in Durran (2010, his section 8.2.5). The pressure equations arising for the other methods are solved in a similar manner. To stabilize the explicit step in the T2$\theta$–LF scheme, the terms on the right-hand side of (39)–(41) are integrated using a forward time step over the interval $2\Delta t$. This low-accuracy forward step is neither required nor used with the other IMEX schemes. The starting stages (one or two in the case of two-step and three-step methods, respectively) are computed using the third-order IMEX additive Runge–Kutta method of Kennedy and Carpenter (2003).

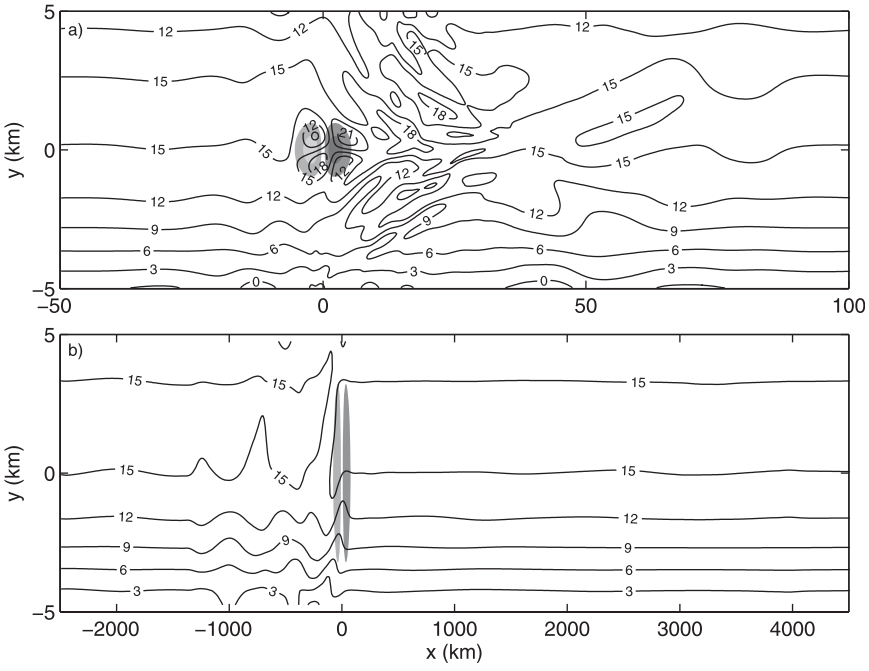


FIG. 9. Contours of the horizontal velocity at $t = t_d$ in the central portion of the domain for (a) case NH and (b) case H. Gray shades show contours of $\psi$ with steps in the grayscale at $\pm 5$ and $\pm 15$ m$^2$ s$^{-2}$ in case NH and $\pm 1$ m$^2$ s$^{-2}$ in case H.

Figure 9 shows contours of the $u$ field at time $t_d$ in a central portion of the full domain for the reference solution for cases NH and H. Also shown by gray shading are contours of the $\psi$ field. The reference solution was computed with a fully explicit fourth-order Runge–Kutta scheme using a very short time step. The time $t_d$ is well before the moment when the evolving gravity waves begin to wrap around the domain through the periodic lateral boundaries. It is perhaps counterintuitive that the forcing projects most strongly onto the upstream-propagating mode in case H, but this was easy to verify analytically in a separate constant-wind speed simulation with $u_0 = 8$ m s$^{-1}$ (not shown).

The accuracy of these semi-implicit methods for case NH is compared in Fig. 10, which shows the relative error in $b$ plotted on a log–log scale as a function of the Courant number associated with horizontal advection, $\max_{x,z} u(t_d)\Delta t/\Delta x$. The relative error is evaluated as the RMS difference between the $b$ field at $t = t_d$ computed by each semi-implicit method and the result obtained from the reference solution $b_r$, normalized by the RMS value of $b_r$.

Results for schemes that have seen previous use are given in Fig. 10a. At all but the smallest CFL number (which may be of little practical importance) the best results are obtained using the T2$\theta$–LF method with the RAW filter and no off-centering of the trapezoidal time difference [i.e., $(\theta, \gamma, \sigma) = (0.5, 0.2, 0.53)$]. The worst accuracy is obtained using RA filtering and the T2$\theta$–LF method with $\theta = 0.6$ while implicitly updating the buoyancy-forcing terms, which are the terms in (40) and (41) that are identical to the those labeled b in (19) and (20). Setting $\theta = 0.5$ reduces the error, but still yields a first-order scheme because of the influence of the RA filter. When $\theta = 0.5$, treating the buoyancy explicitly instead of implicitly with the T2$\theta$–LF–RA method has no impact on accuracy (cf. the squares and the thick gray line), but if $\theta = 0.6$, switching from implicit to explicit differencing for the buoyancy reduces the error to almost the same values obtained when $\theta = 0.5$ (cf. the diamonds and the solid black line). Evidently, off-centering the trapezoidal time differencing degrades accuracy much more than the use of the RA filter. Finally, unlike the first-order time-filtered T2$\theta$–LF methods, the BDF2–BX2 scheme exhibits second-order convergence, but it does not actually yield more accurate results than the T2$\theta$–LF–RAW method unless the advective CFL number is very small.

Figure 10b shows the performance of the new methods. At a given time step, the smallest errors are produced when buoyancy is treated explicitly using AI2*–AB3 or BI2*–BX3*, both of which feature third-order accurate explicit schemes. In fact, the overall convergence rate for these two methods appears to be third order, which is surprising since even when the buoyancy is explicit, the pressure gradient and divergence terms are still

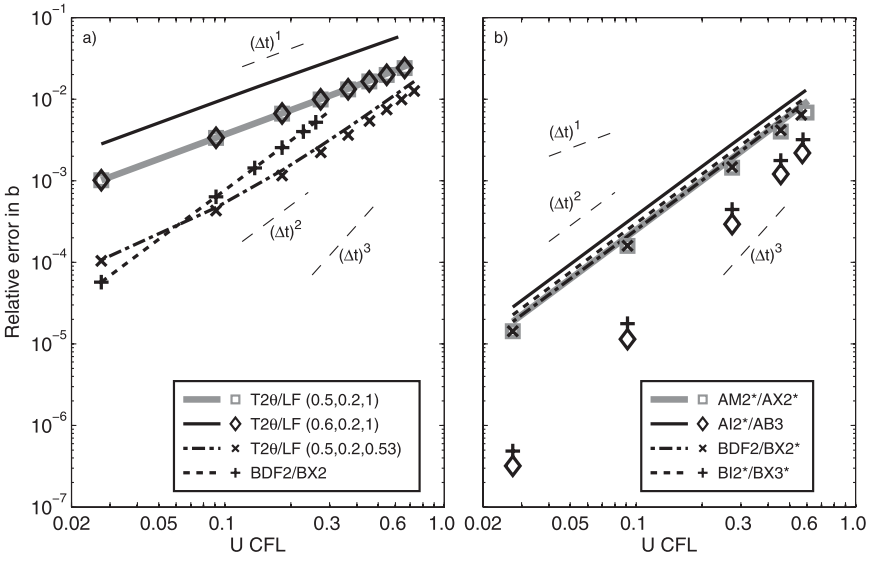


FIG. 10. Log–log plot of the error in the buoyancy field as a function of advective Courant number for the several of the methods listed in Table 1 for case NH. The curves show the result when buoyancy is treated implicitly; the symbols show the results when the buoyancy terms are approximated using the explicit part of the scheme. The lines–symbols terminate at the largest advective CFL number for which each method is stable. Thin dashed lines show the slopes corresponding to first-, second-, and third-order convergence. The triplet of numbers after the T2$\theta$–LF methods denote the values of ($\theta$, $\gamma$, $\sigma$).

integrated using second-order implicit schemes. At the same advective CFL number of 0.57, the T2$\theta$–LF–RAW scheme, which is the best leapfrog-trapezoidal method, generates roughly 4 times the error of the AI2*–AB3 method, and this difference increases rapidly as the time step is further reduced. If the buoyancy is treated implicitly, all the new schemes behave similarly, but the best are BDF2–BX2* and AM2*–AX2*, which use superior implicit schemes. Again, these new schemes deliver more accuracy at a given time step (advective CFL number) than those shown in Fig. 10a, although when the buoyancy is implicit, they are only slightly superior to the T2$\theta$–LF–RAW method at the largest CFL numbers.

Each of the curves shown in Fig. 10 terminates at the largest value of $\max_{x,z}[u(t_d)]\Delta t/\Delta x$ for which the solutions could integrated to $t_f$ without any sign of incipient instability. These empirically determined stability limits are listed in Table 4 to within an accuracy of $\pm 0.01$. In case NH, the largest stable time step is permitted by the RAW-filtered T2$\theta$–LF method with buoyancy treated implicitly. The maximum stable advective CFL numbers permitted by the new Adams and backward IMEX methods are smaller than that for the RAW-filtered T2$\theta$–LF method by a factor of about 0.8. The BDF2–BX2 scheme requires much smaller time steps than any of the other methods.

Figure 11 gives the same information as Fig. 10 for case H. In case H, the basic behaviors of all the methods remain similar to those discussed in case NH, although the gravity waves travel much faster. As a consequence, the maximum advective CFL number for which stable integrations can be performed when the buoyancy is explicit is roughly 1/5 of that which can be used in case NH (recall the logarithmic scaling of the axes in these plots, and see also Table 4). It is therefore, not likely practical to treat the buoyancy explicitly in problems similar to case H. When buoyancy is implicit, the magnitude of the high-frequency (gravity wave) forcing over the low-frequency (advective) forcing is greater in case

TABLE 4. Maximum advective CFL numbers at which each method remains stable. Explicit and implicit refer to the treatment of the buoyancy forcing in (40) and (41), which are identical to the terms labeled b in (19) and (20). The triplet of numbers after the T2$\theta$–LF methods denote the values of ($\theta$, $\gamma$, $\sigma$). Values are empirically determined to within $\pm 0.01$.

| | Case NH | | Case H | |
|---|---|---|---|---|
| Method | Explicit | Implicit | Explicit | Implicit |
| BDF2–BX2 | 0.26 | 0.30 | 0.03 | 0.22 |
| T2$\theta$–LF (0.5, 0.2, 1) | 0.66 | 0.69 | 0.08 | 0.75 |
| T2$\theta$–LF (0.6, 0.2, 1) | 0.66 | 0.62 | 0.13 | 0.75 |
| T2$\theta$–LF (0.5, 0.2, 0.53) | 0.73 | 0.73 | 0.08 | 0.78 |
| MCN–AX2+ | 0.57 | 0.57 | 0.05 | 0.47 |
| AM2*–AX2* | 0.60 | 0.61 | 0.13 | 0.75 |
| AI2*–AB3 | 0.57 | 0.59 | 0.11 | 0.70 |
| BDF2–BX2* | 0.57 | 0.59 | 0.11 | 0.66 |
| BI2*–BX3* | 0.58 | 0.59 | 0.11 | 0.72 |

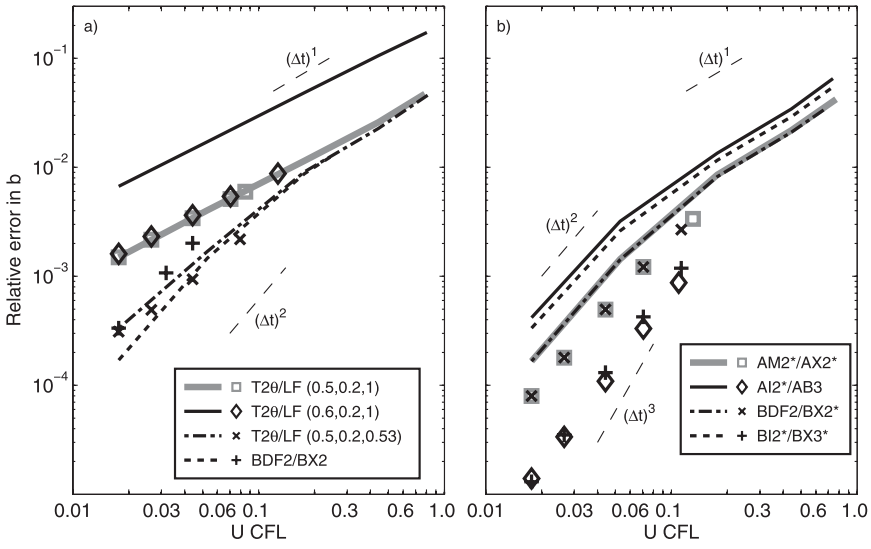


FIG. 11. As in Fig. 10, but for case H.

H than in case NH, and therefore the maximum stable CFL numbers in case H are larger than those in case NH (consistent with the stability regions in Figs. 5 and 6). The largest advective CFL number is again permitted by the RAW-filtered T2$\theta$–LF method, but that for the AM2*–AX2* method is only smaller by a factor of 0.96. Note also, that when buoyancy is treated implicitly, the superiority of the new Adams and backward schemes with good implicit parts (AM2*–AX2* and BDF2–BX2*) over their cousins with explicit third-order parts is more pronounced than in case NH.

## 5. Discussion and conclusions

We have proposed two new families of IMEX multistep methods for the efficient solution of fast-wave–slow-wave problems in which the fast waves need not be accurately simulated. One family is based on Adams methods, the other on backward differencing schemes. In both cases the implicit parts of the schemes are two-step second-order $A$-stable methods. The explicit parts are second-order three-step methods, except for two that are third order. We focused on four members of these two families, the two with nominally the best implicit schemes: AM2*–AX2* and BDF2–BX2*, and the two with third-order explicit parts: AI2*–AB3 and BI2*–BX3*.

These new schemes were compared against previously proposed versions of the IMEX leapfrog-trapezoidal method and the BDF2–BX2 scheme in three contexts: the oscillation equation with separate high- and low-frequency forcing, and both the linearized and the nonlinear ''compressible Boussinesq'' system. When it is practical to approximate the buoyancy forcing terms with the explicit part of the IMEX scheme, AI2*–AB3 and BI2*–BX3*appear to give considerably more accurate results than the other methods, while still permitting time steps with advective CFL numbers only slightly smaller than the best leapfrog-trapezoidal scheme. When buoyancy is implicit, the improvement obtained using the best new schemes (which in the case with implicit buoyancy are AM2*–AX2* and BDF2–BX2*) is less pronounced; in particular, the RAW-filtered leapfrog-trapezoidal method performed almost as well and allowed a slightly larger time step.

One additional advantage of the new methods is that the explicit parts of these schemes are capable of naturally approximating terms arising from dissipation or model physics, whereas such terms must be incorporated in the explicit part of leapfrog-trapezoidal methods using a first-order Euler step over a time interval of $2\Delta t$. Finally, we note that off-centering the trapezoidal update in the T2$\theta$–LF method with $\theta = 0.6$ gave very inaccurate results in both cases H and NH. The damping produced by such off-centering is not very scale selective, and the numerical results for this scheme were notably worse than all the others.

The stability constraints for the previously used BDF2–BX2 method require a much smaller advective CFL number than that for the other schemes. In the context considered here, in which periodic horizontal boundary conditions allow the implicit problem to be solved efficiently using direct methods, this constraint on the time step is a serious disadvantage. On the other hand, in those circumstances where iterative solvers are employed, the overall efficiency of the method depends on the condition

TABLE 5. Influence of the implicit-scheme coefficients on the condition number in the explicit-buoyancy test problem.

| Method | $(\alpha_1/\nu_1)^2$ |
|---|---|
| MCN | 0.316 |
| BDF2 | 0.444 |
| AM2* | 0.562 |
| BI2* | 0.790 |
| T2$\theta$, $\theta = 0.5$ | 1.00 |
| T2$\theta$, $\theta = 0.6$ | 1.44 |
| AI2* | 1.56 |

number of the coefficient matrix arising from the implicit part of the scheme. When buoyancy is treated explicitly, the condition number for the implicit subproblem in our nonlinear test case is very closely proportional to

$$\left(\frac{\nu_1}{\alpha_1}\right)^2 \frac{(c_s \Delta t)^2}{(\Delta x)^2 + (\Delta z)^2}, \tag{43}$$

where $\alpha_1$ and $\nu_1$ are the coefficients of the state variables at the new time level listed for each scheme in Table 1. The condition number is influenced by both the implicit part of the IMEX scheme and by the time step. Giraldo (2005) noted that, provided the condition number is small enough to dramatically reduce the number of iterations required during each implicit step, the most efficient scheme can sometimes be one for which $\nu_1/\alpha_1$ and the maximum time step are both small.

The values of $(\nu_1/\alpha_1)^2$ for the preceding implicit methods are listed in Table 5. The smallest value is associated with the modified Crank–Nicolson scheme MCN of Ascher et al. (1995). The member of the family of stable IMEX Adams schemes for fast-wave–slow-wave problems that uses the MCN scheme is listed in Tables 1 and 4. Among the two-step second-order implicit Adams methods, MCN has the best damping properties at negative infinity [$|A| \to \frac{1}{3}$ as $\Re(\eta) \to -\infty$ in (3)], but its fast-wave–slow-wave stability properties are worse than the schemes created using BDF2 and AM2*, so we have not focused on this method. In problems where the condition number is of primary concern, however, this method might be attractive.

Among the other methods, BDF2 has the next smallest condition number, followed by AM2*. AI2* has the largest condition number, and is the only one of the newly proposed schemes with a condition number larger than the T2$\theta$ schemes. When the condition number is a significant consideration, BI2*–BX3* would be a much better choice than AI2*–AB3 for an IMEX scheme with a third-order explicit step.

In this paper we have endeavored to investigate a large class of IMEX linear multistep methods. Linear multistep methods are one of the most important families of methods for the solution of ordinary differential equations, but they are not the only approach. Another very important approach involves multistage methods, the most prominent of which are Runge–Kutta schemes, and IMEX Runge–Kutta schemes have been used in many advection-diffusion problems. An investigation of IMEX Runge–Kutta schemes for the fast-wave–slow-wave problem is beyond the scope of this paper, but has recently been discussed by Ullrich and Jablonowski (2012).

*Acknowledgments.* The authors benefited from discussions with Frank Giraldo and from comments by the anonymous reviewers. This research was supported by the National Science Foundation through Grant ATM-0836316 and the Office of Naval Research through Contract N00173-10-1-G033.

## REFERENCES

Ascher, U. M., S. J. Ruuth, and B. T. R. Wetton, 1995: Implicit-explicit methods for time-dependent partial differential equations. *SIAM J. Numer. Anal.,* **32,** 797–823.

Asselin, R., 1972: Frequency filter for time integrations. *Mon. Wea. Rev.,* **100,** 487–490.

Bannon, P. R., 1996: On the anelastic approximation for a compressible atmosphere. *J. Atmos. Sci.,* **53,** 3618–3628.

Benoit, R., M. Desgagné, P. Pellerin, S. Pellerin, Y. Chartier, and S. Desjardins, 1997: The Canadian MC2: A semi-Lagrangian, semi-implicit wideband atmospheric model suited for finescale process studies and simulation. *Mon. Wea. Rev.,* **125,** 2382–2415.

Dahlquist, G. G., 1963: A special stability problem for linear multistep methods. *BIT Numer. Math.,* **3,** 27–43.

Durran, D. R., 1989: Improving the anelastic approximation. *J. Atmos. Sci.,* **46,** 1453–1461.

——, 1991: The third-order Adams–Bashforth method: An attractive alternative to leapfrog time differencing. *Mon. Wea. Rev.,* **119,** 702–720.

——, 2008: A physically motivated approach for filtering acoustic waves from the equations governing compressible stratified flow. *J. Fluid Mech.,* **601,** 365–379.

——, 2010: *Numerical Methods for Fluid Dynamics: With Applications in Geophysics*. Springer, 516 pp.

Evans, K. J., M. A. Taylor, and J. B. Drake, 2010: Accuracy analysis of a spectral element atmospheric model using a fully implicit solution framework. *Mon. Wea. Rev.,* **138,** 3333–3341.

Fornberg, B., and T. A. Driscoll, 1999: A fast spectral algorithm for nonlinear wave equations with linear dispersion. *J. Comput. Phys.,* **155,** 456–467.

Frank, J., W. Hundsdorfer, and J. G. Verwer, 1997: On the stability of implicit-explicit linear multistep methods. *Appl. Numer. Math.,* **25,** 193–205.

Giraldo, F. X., 2005: Semi-implicit time-integrators for a scalable spectral element atmospheric model. *Quart. J. Roy. Meteor. Soc.,* **131,** 2431–2454, doi:10.1256/qj.03.218.

——, M. Restelli, and M. Läuter, 2010: Semi-implicit formulations of the Navier–Stokes equations: Application to

nonhydrostatic atmospheric modeling. *SIAM J. Sci. Comput.,* **32,** 3394–3425.

Karniadakis, G. E., M. Israeli, and S. A. Orszag, 1991: High-order splitting methods for the incompressible Navier-Stokes equations. *J. Comput. Phys.,* **97,** 414–443.

Kennedy, C. A., and M. H. Carpenter, 2003: Additive Runge-Kutta schemes for convection-diffusion-reaction equations. *Appl. Numer. Math.,* **44,** 139–181, doi:10.1016/S0168-9274(02)00138-1.

Klemp, J. B., and R. Wilhelmson, 1978: The simulation of three-dimensional convective storm dynamics. *J. Atmos. Sci.,* **35,** 1070–1096.

Kwizak, M., and A. J. Robert, 1971: A semi-implicit scheme for grid point atmospheric models of the primitive equation. *Mon. Wea. Rev.,* **99,** 32–36.

Lipps, F., and R. Hemler, 1982: A scale analysis of deep moist convection and some related numerical calculations. *J. Atmos. Sci.,* **39,** 2192–2210.

Nevanlinna, O., and W. Liniger, 1978: Contractive methods for stiff differential equations Part I. *BIT Numer. Math.,* **18,** 457–474.

Ogura, Y., and N. A. Phillips, 1962: Scale analysis for deep and shallow convection in the atmosphere. *J. Atmos. Sci.,* **19,** 173–179.

Robert, A. J., 1966: The integration of a low order spectral form of the primitive meteorological equations. *J. Meteor. Soc. Japan,* **44,** 237–244.

Tapp, M. C., and P. W. White, 1976: A non-hydrostatic mesoscale model. *Quart. J. Roy. Meteor. Soc.,* **102,** 277–296.

Tatsumi, Y., 1983: An economical explicit time integration scheme for a primitive model. *J. Meteor. Soc. Japan,* **61,** 269–287.

Ullrich, P., and C. Jablonowski, 2012: Operator-split Runge–Kutta–Rosenbrock methods for nonhydrostatic atmospheric models. *Mon. Wea. Rev.,* **140,** 1257–1284.

Varah, J. M., 1980: Stability restrictions on second order, three level finite difference schemes for parabolic equations. *SIAM J. Numer. Anal.,* **17,** 300–309.

Wicker, L. J., and W. C. Skamarock, 2002: Time-splitting methods for elastic models using forward time schemes. *Mon. Wea. Rev.,* **130,** 2088–2097.

Williams, P. D., 2009: A proposed modification to the Robert–Asselin time filter. *Mon. Wea. Rev.,* **137,** 2538–2546.

——, 2011: The RAW filter: An improvement to the Robert–Asselin filter in semi-implicit integrations. *Mon. Wea. Rev.,* **139,** 1996–2007.